Superconducting ‘twin’ qubit

I. V. Antonov,[1,2] R. S. Shaikhaidarov,[1,4] V. N. Antonov,[3,1,4] and O. V. Astafiev[3,1,2,4]
[1]*Royal Holloway, University of London, Egham, TW20 0EX, United Kingdom*
[2]*National Physical Laboratory, Hampton Road Teddington, TW11 0LW, United Kingdom*
[3]*Skolkovo Institute of Science and Technology, Nobel str. 3, Moscow, 143026, Russia*
[4]*Moscow Institute of Physics and Technology, 29 Institutskiy per., 141700 Dolgoprudny, Moscow Region, Russia*

(Received 2 March 2020; revised 4 August 2020; accepted 25 August 2020; published 21 September 2020)

We study a flux qubit consisting of a symmetrical pair of superconducting loops, with two Josephson junctions in each, joined by a common Josephson junction—a ‘twin’ flux qubit. The qubit is capacitively coupled to a transmission line, which allows us to characterize the spectrum of the device by measuring the scattering of propagated electromagnetic waves. We perform a detailed analytical analysis of the double-loop system, revealing its properties, and compare experimental results with numerical simulations. At half-flux quantum bias of both loops, the qubit is protected against global and local magnetic field fluctuations with much less sensitivity to the global field in the second order. The system selection rules allow even-odd transitions and prohibit transitions between even-even or odd-odd levels due to the symmetry of the device.

DOI: 10.1103/PhysRevB.102.115422

I. INTRODUCTION

Superconducting qubits are among the most promising platforms for quantum computing technology. Typical qubits are on-chip aluminium structures with Josephson junctions (JJs), whose geometry can be designed to select an operating energy, state transition rates, and sensitivity required for a particular environment. Over the past decade they have carried out the functionality of a transistor [1–4]—where a control field was used to pass or block a probe field at a different frequency, multiplexer [5]—two input signals can be mixed to controllably generate a single output signal and serial bus [6]. Superconducting qubits can be fabricated using standard nanofabrication techniques and integrated at scale into quantum circuits [7].

One of the inherent limitations, which is encountered with superconducting qubits, is a coherence time τ_{dec}, beyond which quantum information becomes lost. In early qubits the decoherence time was in the range of a few ns. Two main sources of decoherence are charge and flux fluctuations in the vicinity of the qubit. Charge fluctuations are particular harmful for the qubits, where the charging energy E_C is large. In flux qubit architectures the JJ energy E_J dominates over the charging energy ($E_J/E_C \gg 1$), which lowers the device’s charge sensitivity [8–10]. A family of flux qubit designs have led to improvement of the coherence times: capacitively-shunted flux qubit [11,12], 4-JJ qubit [13].

Here we investigate experimentally a ‘twin’ qubit, consisting of two symmetrical flux qubits, linked by a common α-JJ, Fig. 1. The original investigation was motivated by the weak flux dependence of the system transition energy when it is biased to the degeneracy point ($\Phi_0/2$) in each loop. Compared to the original flux qubit, the energy levels of the ‘twin’ qubit are very flat. In a recent publication, a chain of 15 such qubits was placed into a coplanar waveguide to demonstrate flux-tuneable transmission of microwaves [14]. In our work we isolate one of these ‘twin’ qubits and perform a detailed characterization. Experimental study of the transmission spectrum confirms weak dependence on the global-flux anharmonicity with respect to the $|0\rangle \leftrightarrow |1\rangle$ and $|1\rangle \leftrightarrow |2\rangle$ transitions ($|0\rangle$, $|1\rangle$, $|2\rangle$ correspond to the ground, first-excited, second-excited states). Simulations further indicate some level of protection against local-flux fluctuations.

II. DEVICE LAYOUT AND MEASUREMENTS SETUP

The sample is fabricated on an undoped silicon substrate, which is pre-patterned with 100 nm Au ground planes. We use electron beam lithography and a shadow evaporation technique to fabricate the qubit shown in Fig. 1(a). The qubit consists of five JJs integrated into two symmetrical superconducting loops. The JJs have a layered structure of Al (20 nm)-AlO$_x$-Al (30 nm). The energy and capacitance of the central JJ is a factor of α larger than for the outside ones, which have dimensions 400×200 nm^2. The coplanar transmission line with impedance $Z_0 \sim 50\ \Omega$ runs to the opening between the ground planes in the center of the chip. The qubits are coupled to the transmission line through T-shaped capacitors. An external magnetic field is applied to change magnetic flux linked through the almost-identical loops.

The sample is mounted on a holder at the 13 mK stage of a dilution refrigerator. A superconducting shield is used

---

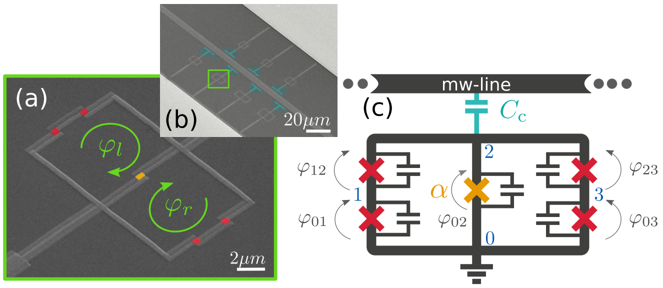

FIG. 1. Geometry of a ‘twin’ qubit: (a) Scanning electron microscope image of the ‘twin’ qubit. The Al-AlO$_x$-Al JJs are highlighted in red and yellow. φ_l and φ_r are phases induced in the left and right loops by an external magnetic field. (b) Each of the qubits is coupled to the transmission line with a T-shaped capacitor (light blue). (c) The ‘twin’ qubit is a symmetrical arrangement of two individual flux qubits [8] sharing the central JJ. The qubit has four islands, which are labeled with Cooper pair (CP) occupation $\vec{n} = |n_1, n_2, n_3\rangle$, and phases across its junctions: φ_{ij}, where i and j are the island indices 0, 1, 2, or 3. The central junction is geometrically a factor α larger than the outer ones, resulting in energies αE_C and αE_J.

to screen the holder from stray magnetic fields. The RF lines connected to the sample have attenuators for thermalization: −50 dBm at room temperature, −10 dBm on the 800 mK stage, −30 dBm on dilution-chamber state (≈13 mK). We attach a circulator on the output line for isolation. The transmitted signal is amplified by approximately +35 dBm on the 4 K stage and by +35 dBm at room temperature. This set of attenuators and amplifiers facilitate power conversion between the laboratory equipment and the qubit. Prior to characterizing the qubit, we took the microwave transmission spectrum with the qubit detuned and corrected all measurements by subtracting this background transmission profile. Our primary goal is to study the operation of the qubit in the vicinity of a double degeneracy point ($\Phi_0/2$), find the intrinsic energy structure and compare with a numerical model of the system.

III. MEASUREMENT RESULTS

We study the energy spectrum of the ‘twin’ qubit by measuring transmission of coherent waves while sweeping the biasing magnetic flux. The $|0\rangle \leftrightarrow |1\rangle$ transition is mapped with a network analyzer which measures the transmission of signal $\omega_{\rm NA}$ through the system. Away from resonance the signal passes through the circuit without any interaction with the qubit so that the transmission is close to 100%.

Only near resonance ($\omega_{\rm NA} \approx \omega_{10}$) does the qubit exchange photons with the driving field as it evolves between the ground and excited states. The qubit emits a wave that is in antiphase with the driving field [1], so that the destructive interference in the output line results in a transmission dip, see Fig. 2(a) inset. The transmission coefficient is $t = 1 - r_0/(1 - i\delta\omega/\Gamma_2)$, where $\delta\omega = \omega_{NA} - \omega_{21}$, $r_0 = \Gamma_1^r/2\Gamma_2$ is an effective reflection coefficient, Γ_1^r is the radiative decay from the qubit to the line, and Γ_2 is the total dephasing [1,15] (see Supplemental Material note I [16]). The inset of Fig. 2(a) shows the power transmission spectrum obtained in a weak driving limit, when it takes the simplified form $|t|^2 \approx 1 - 2r_0/[1 - (\delta\omega/\Gamma_2)^2]$.

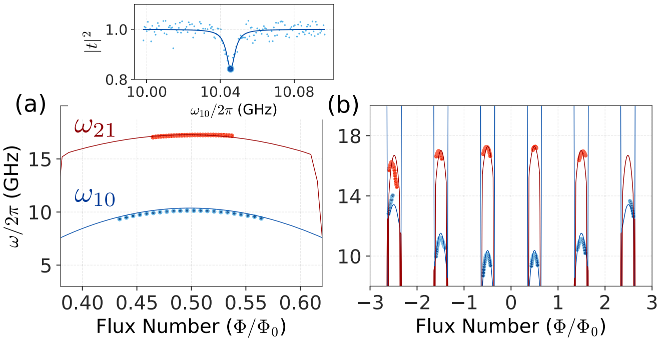

FIG. 2. Spectrum of the quantum system: (a) The resonance frequencies (ω_{10}) in the vicinity of $\Phi_0/2$ (blue points). An inset exemplifies the power transmission coefficient $|t|^2$ for the $|0\rangle \leftrightarrow |1\rangle$ transition, taken in the weak driving limit. The transition frequencies ω_{21} (red) are obtained in a two-tone measurement. (b) The spectrum measured in a wide flux bias range. Experimental data (circles) are compared with simulations (solid lines) for ω_{10} (blue) and ω_{21} (red). Asymmetry in the flux penetrating the left and right loops results in the gradual change of transition frequencies with every Φ_0 period: ω_{10} creeps up, while ω_{21} creeps down, breaking the usual periodicity seen in flux qubits.

Fitting the dip we find $\Gamma_2/2\pi \approx 3.5$ MHz and $\Gamma_1^r/2\pi \approx 0.6$ MHz.

The transmission minimum at different magnetic fields maps out the qubit's ground-to-excited-state frequency (ω_{10}) in Fig. 2(a). Such a spectrum is observed in the vicinity of external flux bias $\Phi \approx \Phi_0/2$ for all samples. Because of a small asymmetry, $\eta \approx 1$, the phases induced through the left and right loops can be slightly different: $\varphi_l = \Phi/2\pi$ and $\varphi_r = \eta\Phi/2\pi$. This results in gradual change of the resonant frequency at larger magnetic fields, Fig. 2(b).

The $|1\rangle \leftrightarrow |2\rangle$ transition (ω_{21}) is mapped using spectroscopy with two tones. The network analyser probes signals at ω_{10}, while an additional generator sweeps a second frequency, $\omega_{\rm GEN}$. Whenever the second tone from the generator hits the $|1\rangle \rightarrow |2\rangle$ transition ($\omega_{\rm GEN} = \omega_{21}$), the qubit undergoes a ladder of excitations, $|0\rangle \xrightarrow{\omega_{10}} |1\rangle \xrightarrow{\omega_{21}} |2\rangle$, depopulating states $|0\rangle$ and $|1\rangle$. Because of this depopulation, the probe signal at ω_{10} is modified. This identifies ω_{21}, which is mapped with red circles, see Fig. 2. One can note that the qubit has a large anharmonicity of more than 7.5 GHz in the two lowest transitions.

IV. JOSEPHSON POTENTIAL: STABILITY DIAGRAMS

Each JJ contributes $E_{Jij}[1 - \cos(\varphi_{ij})]$ to a Josephson potential. The loops are biased by an external magnetic field, which can be accounted for as externally induced phases in the left (φ_l) and right (φ_r) loops, see Fig. 1. Therefore $\varphi_{01} + \varphi_{12} - \varphi_{02} = -\varphi_l$ and $\varphi_{02} - \varphi_{32} - \varphi_{03} = -\varphi_r$ are the phase-bounding conditions due to flux quantization. The Josephson potential of our device can be written as

$$\begin{aligned} U = {} & E_J[4 + \alpha - \alpha\cos\varphi_{02} - \cos\varphi_{01} - \cos\varphi_{03} \\ & - \cos(\varphi_{02} - \varphi_{01} - \varphi_l) - \cos(\varphi_{02} - \varphi_{03} + \varphi_r)]. \quad (1) \end{aligned}$$

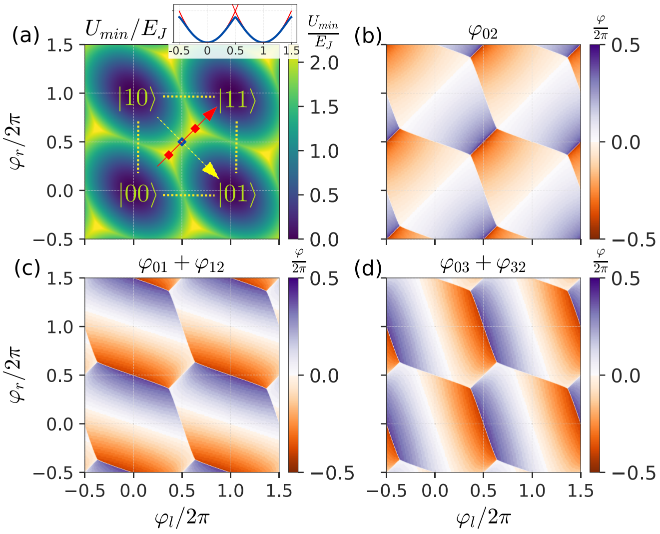

FIG. 3. Stability diagrams of the system: (a) The minimal value of Josephson potential is plotted as a function of externally induced phase in the left (φ_l) and right (φ_r) loops. The stable flux configurations are denoted as $|00\rangle$, $|01\rangle$, $|10\rangle$, and $|11\rangle$. When the loops are symmetrically biased, in the case of a uniform global magnetic field and identical loop areas, the potential takes values along the red arrowed line. An inset shows the energies along the dashed yellow line. The blue curve is the minimized potential and the red curves are parabolic approximations for $|01\rangle$ and $|10\rangle$ flux configurations. Red diamonds mark the ends of the $|01\rangle - |10\rangle$ degeneracy line. (b)–(d) show phases φ_{02}, $\varphi_{01}+\varphi_{12}$, and $\varphi_{03}+\varphi_{32}$. The abrupt phase change by $\sim 2\pi$ corresponds to a flux quantum jumping through the junctions.

Now we will discuss some properties of the potential. Figure 3(a) shows the minimal value of the potential energy ($U_{\min}(\varphi_l, \varphi_r) = \min_{\varphi_{01},\varphi_{12},\varphi_{03}} U$), energetically favorable for the system, as a function of the external phases. The corresponding phases assumed on the JJs are shown in Figs. 3(b)–3(d). Figures 3(c) and Fig. 3(d) show phases in the left and right arms, $\varphi_{01}+\varphi_{12}$ and $\varphi_{03}+\varphi_{32}$. Note that $\varphi_{01}=\varphi_{12}$ and $\varphi_{03}=\varphi_{32}$, as it is expected that the same current flows in junctions situated sequentially on a branch, and $I_{ij} = I_{cij}\sin\varphi_{ij}$, where I_{cij} is the critical current across junction ij. All the patterns are 2π periodic in φ_l and φ_r. Together, the figures demonstrate that there are hexagonal cells centered at $\varphi_l = 2\pi n_L$ and $\varphi_r = 2\pi n_R$, where n_L and n_R are integer numbers. Within the cells, phases vary smoothly as a function of φ_l and φ_r and then may abruptly switch at the boundaries of the cells.

The abrupt change of phase by 2π at the boundaries of the cells corresponds to a flux quantum (Φ_0) jumping in or out of the loops. More precisely, in Fig. 3(c), varying φ_l at fixed φ_r (e.g., $\varphi_r = 0$) results in the phase jump in the left shoulder of the structure when the total phase ($\varphi_{01}+\varphi_{12}$) flips from $-\pi$ to π close to $\varphi_l = \pi + 2\pi n_L, n_L \in \mathbb{Z}$. This corresponds to movement of a flux quantum into the left loop. Similarly, a flux quantum movement occurs in the right loop close to $\varphi_r \approx \pi + 2\pi n_R, n_R \in \mathbb{Z}$; the flux in the right branch ($\varphi_{03}+\varphi_{32}$) is flipped from $-\pi$ to π, see Fig. 3(d).

The most interesting process for us is the motion of the flux quantum between the loops without changing the total flux number in the system. Figure 3(b) shows phase φ_{02} abruptly changing from π to $-\pi$, when moving along the dashed yellow line. This corresponds to a flux quantum jumping from the right loop directly into the left loop. We denote energetically favorable configurations with the ‘stable’ flux states $|n_L n_R\rangle$. For example, $|00\rangle$ denotes the favorable state of the system in the cell centered at $\varphi_l = 0$ and $\varphi_r = 0$. Moving through a boundary of this cell results in a new ‘stable’ flux configuration, which is labeled in Fig. 3(a) for four of the cells.

We will now consider properties of the Josephson potential in cells centered at $\{\varphi_l/2\pi, \varphi_r/2\pi\} = \{n_L, n_R\}$. The minimal values of the Josephson potential can be found from $\partial U/\partial\varphi_{ij} = 0$. Differentiating it in φ_{01} and φ_{03} and applying the phase-bounding conditions in the loops, we find $\varphi_{01} = \varphi_{12} = \frac{\varphi_{02}-\varphi_l}{2} + \pi n_L$ and $\varphi_{03} = \varphi_{32} = \frac{\varphi_{02}+\varphi_r}{2} - \pi n_R$ (see Supplemental Material note IIA [16]). The minimized Josephson energy [Eq. (1)] reads

$$U_{\min}(n_L, n_R) = E_J\bigg[4 + \alpha - 2(-1)^{n_L}\cos\left(\frac{\varphi_{02}-\varphi_l}{2}\right) - 2(-1)^{n_R}\cos\left(\frac{\varphi_{02}+\varphi_r}{2}\right) - \alpha\cos\varphi_{02}\bigg]. \quad (2)$$

Next, $\partial U/\partial\varphi_{02} = 0$ results in

$$(-1)^{n_L}\sin\left(\frac{\varphi_{02}-\varphi_l}{2}\right) + (-1)^{n_R}\sin\left(\frac{\varphi_{02}+\varphi_r}{2}\right) + \alpha\sin\varphi_{02} = 0. \quad (3)$$

This condition is equivalent to the Kirchhoff’s law for currents in our system. The phase behavior at least in the vicinity of the cell centers can be found from the series expansion of this expression up to the first order (see Supplemental Material note IIB [16]), which results in

$$\varphi_{02} \approx \frac{\varphi_l - \varphi_r - 2\pi(n_L - n_R)}{2(1+\alpha)}. \quad (4)$$

Substituting Eq. (4) into Eq. (2), and expanding up to second order around the center of the cells (see Supplemental Material note IIC [16]), we can draw approximated potentials. The blue curve in the inset of Fig. 3(a) shows the potential along the yellow dashed line ($\varphi_+ = \pi$, where $\varphi_+ = \frac{\varphi_l+\varphi_r}{2}$) minimized in all φ_{ij}. Two red parabolic curves are taken from the series expansion of $U_{\min}$, where the left parabola is for $n_L = 0$, $n_R = 1$ (state $|01\rangle$) and the right one is for $n_L = 1$, $n_R = 0$ (state $|10\rangle$). This approximation case is equivalent to the replacement of the Josephson junctions by linear inductances. The parabolic approximations slightly deviate from the exact calculations only at $\varphi_l \approx \pi$ (the boundary of the cell).

From Fig. 3(a) we can also identify a ‘triple-point,’ where energies of three configurations $|n_L, n_R\rangle$, $|n_L, n_R+1\rangle$, and $|n_L+1, n_R\rangle$ are degenerated—that is $U(n_L, n_R) = U(n_L, n_R+1) = U(n_L+1, n_R)$. For the $|00\rangle$, $|01\rangle$, and $|10\rangle$ states, the point lies on the red arrowed line ($\varphi_- = 0$, where $\varphi_- = \frac{\varphi_l-\varphi_r}{2}$) of Fig. 3. We denote the position of the ‘triple-point’ as $\varphi_l = \varphi_r = \varphi_T$. Using Eq. (2) and Eq. (3) to minimize $U(0,0)$, we find that $\varphi_{02} = 0$ and, therefore, $U_{\min}(0,0)/E_J = 4 - 4\cos\frac{\varphi_T}{2}$. Similarly the condition for minimal $U(0,1)$ is found to be $\sin\frac{\varphi_{02}}{2} = \frac{1}{\alpha}\sin\frac{\varphi_T}{2}$ and $U_{\min}(1,0)/E_J = 4 - \frac{2}{\alpha}\sin^2\frac{\varphi_T}{2}$. The condition $U_{\min}(0,0) = U_{\min}(0,1) = U_{\min}(1,0)$

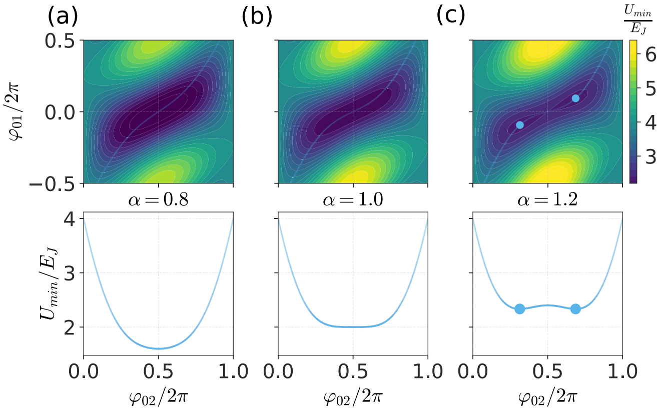

FIG. 4. Potential minimum at the ($\varphi_l = \pi, \varphi_r = \pi$) degeneracy point: The plots show 2D Josephson potential in φ_{02}-φ_{01} coordinates and 1D potentials along the minimum as a function of φ_{02} (light blue line) for: (a) $\alpha = 0.8$; (b) $\alpha = 1.0$; (c) $\alpha = 1.2$. A double well emerges for $\alpha > 1.0$ (light blue points).

brings us to the solution $\varphi_T = 2\arccos(\sqrt{1+\alpha^2} - \alpha)$ (see Supplemental Material IID [16]). For $\alpha = 1$, $\varphi_T/2\pi \approx 0.36$ and the total length of the degeneracy $|01\rangle - |10\rangle$ line is $\Delta\varphi_l/2\pi = \Delta\varphi_r/2\pi \approx 0.28$.

V. ANHARMONIC JOSEPHSON POTENTIALS

Next we consider the Josephson potential in the φ_{ij} space at fixed φ_l and φ_r. We are interested in the region along the red arrowed line in Fig. 3(a), where states $|01\rangle$ and $|10\rangle$ are degenerated. Because the potential is a function of three independent variables (φ_{01}, φ_{02}, and φ_{03}), for visualization on a 2D plot we reduce the number of variables by excluding φ_{03}. Figures 4(a)–4(c) show $U(\varphi_{01}, \varphi_{02})/E_J = \min_{\varphi_{03}}(U/E_J)$ at $\varphi_l = \varphi_r = \pi$ for three different α parameters ($\alpha = 0.8$, $\alpha = 1.0$, and $\alpha = 1.2$). The bottom plots show the potential along the minimal energies with $U(\varphi_{02})/E_J = \min_{\varphi_{01}} U(\varphi_{01}, \varphi_{02})/E_J$. All phases are defined on a 2π interval, however, here, we shift φ_{02} along the x axis from $[-\pi;\pi]$ to $[0;2\pi]$ to center on the potential minimum. The 2π-phase flip from $\varphi_{02} = -\pi \rightarrow \pi$ (along yellow line in Fig. 3), accompanied by a flux quantum jump, now corresponds to $\varphi_{02} = \pi - 0 \rightarrow \pi + 0$.

In contrast to three and four-junction flux qubits, $\alpha = 1.0$ corresponds to the case when the second order of the potential, at the minimal point, is completely suppressed. With $\alpha < 1$, the potential is anharmonic but with a nonzero second order curvature at the center. And $\alpha > 1$ corresponds to the double well potential case.

Now we analyze the potential analytically at the symmetric point $\varphi_l = \pi$ and $\varphi_r = \pi$ on the boundary of cells $\{0, 1\}$ and $\{1, 0\}$ (blue diamond in Fig. 3). The minimal U corresponds to $\varphi_{03} = \varphi_{32} = \frac{\varphi_{02} \mp \pi}{2}$ and therefore $U = E_J[4 + \alpha - \alpha\cos\varphi_{02} - \cos\varphi_{01} \mp 2\sin\frac{\varphi_{02}}{2} + \cos(\varphi_{02} - \varphi_{01})]$. This is the analytical form of the 2D potentials in Figs. 4(a)–4(c). Furthermore, minimizing in φ_{01} gives $\varphi_{01} = \varphi_{12} = \frac{\varphi_{02} \pm \pi}{2}$ and $U = E_J[4 + \alpha - \alpha\cos\varphi_{02} \mp 4\sin\frac{\varphi_{02}}{2}]$ (see Supplemental Material note IIE [16]). The potential has the minimum (or minima) in the vicinity of $\varphi_{02} = \pi$, which will be labeled as a deviation $\delta\varphi_{02}$, such that $\varphi_{02} = \pi + \delta\varphi_{02}$. Then

$$\min_{\varphi_{01},\varphi_{03}}(U) = E_J\left[4 + \alpha + \alpha\cos\delta\varphi_{02} - 4\cos\frac{\delta\varphi_{02}}{2}\right]. \tag{5}$$

When $\delta\varphi_{02}$ is small, both terms are approximated by parabolas, where the first term behaves as if it were classical linear inductance. A series expansion of the potential up to the second order gives $U \approx E_J[2\alpha + (1-\alpha)\frac{\delta\varphi_{02}^2}{2}]$. This means that when $\alpha > 1$, the potential curvature at $\delta\varphi_{02} = 0$ becomes negative and the potential shape turns to double well.

The values of minima can be found again by differentiation of U by φ_{02}, which is simplified to $2\sin\frac{\delta\varphi_{02}}{2}(1 - \alpha\cos\frac{\delta\varphi_{02}}{2}) = 0$. The minima of U are found as

$$\varphi_{02} = \pi, \quad \alpha \leqslant 1$$
$$\varphi_{02} = \pi \pm 2\arccos\frac{1}{\alpha}, \quad \alpha > 1. \tag{6}$$

When $\alpha > 1$, the potential has two minima at $\varphi_{02} = \pi \pm \phi$, where $\phi = 2\arccos\frac{1}{\alpha}$. If we map the phase back into the $[-\pi;\pi]$ range, then $\varphi_{02} \approx -\pi + \phi$ and $\varphi_{02} \approx \pi - \phi$. This means that with small ϕ, the jump of the system from one well to another is accompanied by change of the phase by nearly 2π and therefore a jump a flux quantum through the middle junction.

VI. THE HAMILTONIAN

The charges and potentials on the islands are linked by the capacitance matrix:

$$2e\vec{n} = \boldsymbol{C}\vec{V}. \tag{7}$$

The capacitance matrix in the ‘twin’ qubit topology is (see Supplemental Material note III [16]):

$$\boldsymbol{C} = C\begin{pmatrix} 2 & -1 & 0 \\ -1 & 2+\alpha & -1 \\ 0 & -1 & 2 \end{pmatrix}, \tag{8}$$

where C is the capacitance of the outer JJs. The interaction of the CPs, carrying a charge $\vec{Q} = 2e\vec{n}$, and potentials on their respective islands gives rise to the kinetic energy term (considering vortex motion) of the Hamiltonian:

$$T = E_C C\vec{n}^T\boldsymbol{C}^{-1}\vec{n}, \tag{9}$$

where charging energy is $E_C = (2e)^2/2C$.

The Hamiltonian, $\mathcal{H} = T + U$, is written in the charge basis (see Supplemental Material note IV [16]) with $E_J/h = 91.0$ GHz, $E_C/h = 13.5$ GHz, $\alpha = 1.023$, $\eta = 1.011$, where $\eta = \varphi_r/\varphi_l$. The resulting eigenenergies are compared with the experimental data in Fig. 2(b). Data for ω_{32} is shown in the limited flux range from 0.37 Φ_0 to 0.63 Φ_0, because away from $\Phi = (n + \frac{1}{2})\Phi_0, n \in \mathbb{Z}$, the energy of $|0\rangle \leftrightarrow |1\rangle$ diverges.

The discrepancy between the experimental data and the simulations in Fig. 2(b) can be a result of deviation of the actual qubit parameters from the fitted ones—for example, the JJ in the two arms of the qubit are likely to have small differences after fabrication; at relatively large bias, the actual magnetic field may deviate from what we expect due the influences of trapped vortices in the ground planes.

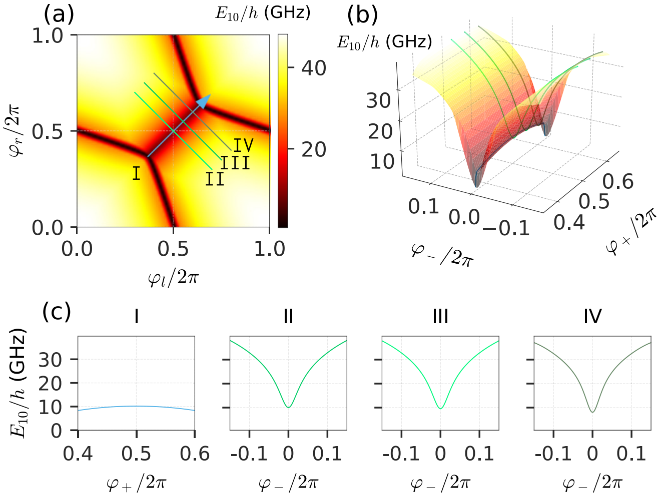

FIG. 5. Energies of ground-to-excited state transitions: (a),(b) Transition energies as functions of external phase biases (φ_l, φ_r, $\varphi_+ = (\varphi_l + \varphi_r)/2$, $\varphi_- = (\varphi_l - \varphi_r)/2$). (c) Transition energies along lines denoted I, II, III, and IV. Curve I shows the transition energy as a function of the global magnetic flux, which increases with φ_+. Curves II, III, and IV show the transition energy as a function of the difference in magnetic fluxes, denoting local flux fluctuations. The qubit is much better protected against the global field fluctuations as curve I has a much smaller curvature.

Importantly, the transition matrix element (d_{02}) is 0 for a wide magnetic flux interval, in contrast with a flux qubit where it happens strictly at the degeneracy point ($\Phi_0/2$). Below we will discuss properties of the dipole elements in details. We estimate the photon emission rate using relationship [1,15] $\Gamma_1^r = (d_{01}C_c)^2\omega Z_0/\hbar$ and found that the previously estimated value ($\Gamma_1^r/2\pi = 0.6$ MHz) can be obtained if we substitute coupling capacitance $C_c = 6$ fF, which is a very reasonable value for our geometry.

VII. TRANSITION ENERGIES IN THE VICINITY OF THE SYMMETRIC POINT

Figure 5 shows the ground-to-excited state transition energies of the qubit as a function of local phase biases φ_l and φ_r. In the ideal case of symmetric bias ($\varphi_l = \varphi_r$) and away from the symmetric point ($\varphi_l = \varphi_r = \pi$), the transition energy varies slowly with the global magnetic field, demonstrated by the flat curve I in Fig. 5(c). In the perpendicular directions to $\varphi_+ = \frac{\varphi_l+\varphi_r}{2} =$ const, which is attributed to the system undergoing completely anticorrelated fluctuations in the two loops (an extreme case of local fluctuations), energy bands have a steep gradient away from the $|01\rangle$-$|10\rangle$ degeneracy line (blue line in Fig. 5), demonstrated by curves II, III, IV in Fig. 5(c).

Numerically, $\partial E_{10}/\partial\varphi_+ = \partial E_{10}/\partial\varphi_- = 0$ at $\varphi_l = \varphi_r = \pi$, but the curvatures characterized by the second derivatives are $\hbar^{-2}\partial^2 E_{10}/\partial\varphi_-^2 \approx -380\ \text{GHz}/\Phi_0^2$ and for the global field $\hbar^{-2}\partial^2 E_{10}/\partial\varphi_+^2 \approx 4\times10^4\ \text{GHz}/\Phi_0^2$. This confirms that although in first order there is no sensitivity to both global and local flux noise, in the second order the qubit is much better protected against the global fluctuations. The local noise can be produced by spin fluctuations on the metallic surfaces [17,18]. Local flux sensitivity can be reduced in expense of anharmonicity, by increasing the junction shunting capacitances [12].

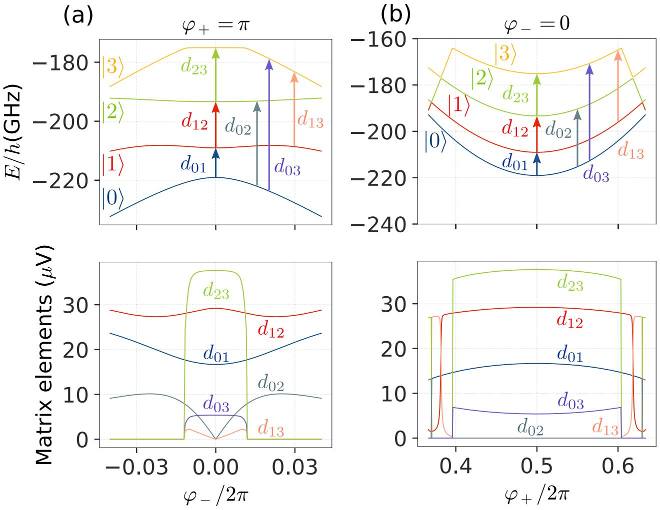

FIG. 6. Energies of the system and the corresponding transition matrix elements: (a) As a function of the local magnetic flux deviations with $\varphi_+ = \pi$. (b) As a function of the global magnetic flux bias with $\varphi_- = 0$.

VIII. TRANSITION MATRIX ELEMENTS

We now analyze the transition matrix elements of the qubit due to excitation from the transmission line through the coupling capacitance. The driving amplitude in transition between levels $|i\rangle$ and $|j\rangle$ can be presented as $\hbar\Omega = V_0 C_c d_{ij}$. The matrix elements $d_{ij} = \langle j|\hat{V}_2|i\rangle$, whose physical meaning is the induced potential on island 2 due to atomic transitions, are calculated and plotted in Fig. 6 for several levels. Here $\hat{V}_2 = (2e)^{-1}\partial\mathcal{H}/\partial n_2$ is the potential operator for the island 2. The calculation of the operator is given in Supplemental Material Note V [16]. Figure 6(a) shows the case $\varphi_+ = \pi$, perpendicular to the $|01\rangle$-$|10\rangle$ degeneracy line.

The general rule is the following: All elements are nonzero at least in some limited range away from the degeneracy point $\varphi_- = 0$. However along the degeneracy line, there are clear selection rules: The transitions between even-odd and odd-even states ($|k\rangle \leftrightarrow |k+1\rangle$, $|k\rangle \leftrightarrow |k+3\rangle$, where k denotes energy levels of the system), particularly transitions between adjacent states, (characterized by $d_{01}, d_{12}, d_{23}, d_{03}$) are allowed, while the transitions between even-even or odd-odd states are prohibited ($d_{02} = d_{13} = 0$). In our device the small asymmetry ($\eta = 1.011$), due to the global magnetic field bias, results in very weak change of the transition energies and dipole moments (Supplemental Material note IV [16]).

IX. DEMONSTRATION OF COHERENT DYNAMICS

Finally, we measure Rabi oscillations, see Fig. 7 by applying short microwave pulses with varied length. The oscillations decay with characteristic time $\tau_{\text{dec}} = 42$ ns. It is consistent with the decoherence time taken from the spectroscopy measurements $\Gamma_2 \approx 1/\tau_{\text{dec}} \approx 2\pi \times 3.8$ MHz.

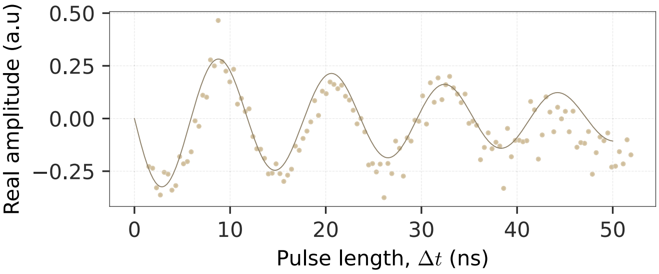

FIG. 7. Rabi oscillations: taken at the degeneracy point by driving the qubit with resonant microwaves pulses for fixed time periods Δt. The decoherence time of $\tau_{\mathrm{dec}} = 42$ ns is extracted from the decay envelope $e^{-\Delta t/\tau_{\mathrm{dec}}}$ of the oscillations.

A relatively short decoherence time in our experiment is not surprising and can be a result of poisoning of the sample with the infrared radiation, and the coupling of the qubit to the two-level oscillators in the substrate, owing to the simplified technology used in the qubit's fabrication. Note also that coherent operation is additionally limited due to strong coupling to the open line.

In conclusion, we have characterized an isolated 'twin' qubit. With this geometry the qubit has weak flux sensitivity at the degeneracy point and strong anharmonicity. We analyzed analytically and numerically properties of our device. The measured energy level structure is well reproduced by the numerical model.

ACKNOWLEDGMENTS

This work was supported by European Union's Horizon 2020 research and innovation programme under Grant Agreement No. 862660/QUANTUM E-LEAPS, Engineering and Physical Sciences Research Council (EPSRC) Grant No. EP/T004088/1, Russian Science Foundation (RSF) Grant No. 20-62-46026.

[1] O. Astafiev, A. M. Zagoskin, A. A. Abdumalikov, Y. A. Pashkin, T. Yamamoto, K. Inomata, Y. Nakamura, and J. S. Tsai, Resonance fluorescence of a single artificial atom, Science **327**, 840 (2010).

[2] I.-C. Hoi, C. M. Wilson, G. Johansson, T. Palomaki, B. Peropadre, and P. Delsing, Demonstration of A Single-Photon Router in the Microwave Regime, Phys. Rev. Lett. **107**, 073601 (2011).

[3] A. A. Abdumalikov, O. Astafiev, A. M. Zagoskin, Y. A. Pashkin, Y. Nakamura, and J. S. Tsai, Electromagnetically Induced Transparency on A Single Artificial Atom, Phys. Rev. Lett. **104**, 193601 (2010).

[4] O. V. Astafiev, A. A. Abdumalikov, A. M. Zagoskin, Y. A. Pashkin, Y. Nakamura, and J. S. Tsai, Ultimate On-Chip Quantum Amplifier, Phys. Rev. Lett. **104**, 183603 (2010).

[5] T. Hönigl-Decrinis, I. V. Antonov, R. Shaikhaidarov, V. N. Antonov, A. Yu. Dmitriev, and O. V. Astafiev, Mixing of coherent waves in a single three-level artificial atom, Phys. Rev. A **98**, 041801(R) (2018).

[6] J.-T. Shen and S. Fan, Coherent Single Photon Transport in A One-Dimensional Waveguide Coupled with Superconducting Quantum Bits, Phys. Rev. Lett. **95**, 213001 (2005).

[7] M. W. Johnson, P. Bunyk, F. Maibaum, E. Tolkacheva, A. J. Berkley, E. M. Chapple, R. Harris, J. Johansson, T. Lanting, I. Perminov, E. Ladizinsky, T. Oh, and G. Rose, A scalable control system for a superconducting adiabatic quantum optimization processor, Supercond. Sci. Technol. **23**, 065004 (2010).

[8] T. P. Orlando, J. E. Mooij, L. Tian, C. H. van der Wal, L. S. Levitov, S. Lloyd, and J. J. Mazo, Superconducting persistent-current qubit, Phys. Rev. B **60**, 15398 (1999).

[9] I. Chiorescu, Coherent quantum dynamics of a superconducting flux qubit, Science **299**, 1869 (2003).

[10] J. E. Mooij, Josephson persistent-current qubit, Science **285**, 1036 (1999).

[11] J. Q. You, X. Hu, S. Ashhab, and F. Nori, Low-decoherence flux qubit, Phys. Rev. B **75**, 140515(R) (2007).

[12] F. Yan, S. Gustavsson, A. Kamal, J. Birenbaum, A. P. Sears, D. Hover, T. J. Gudmundsen, D. Rosenberg, G. Samach, S. Weber, J. L. Yoder, T. P. Orlando, J. Clarke, A. J. Kerman, and W. D. Oliver, The flux qubit revisited to enhance coherence and reproducibility, Nat. Commun. **7**, 12964 (2016).

[13] Y. Qiu, W. Xiong, X.-L. He, T.-F. Li, and J. Q. You, Four-junction superconducting circuit, Sci. Rep. **6**, 28622 (2016).

[14] K. V. Shulga, E. Il'ichev, M. V. Fistul, I. S. Besedin, S. Butz, O. V. Astafiev, U. Hübner, and A. V. Ustinov, Magnetically induced transparency of a quantum metamaterial composed of twin flux qubits, Nat. Commun. **9**, 150 (2018).

[15] Z. H. Peng, S. E. de Graaf, J. S. Tsai, and O. V. Astafiev, Tuneable on-demand single-photon source in the microwave range, Nat. Commun. **7**, 12588 (2016).

[16] See Supplemental Material at http://link.aps.org/supplemental/10.1103/PhysRevB.102.115422 for extended derivations and graphs supporting the main text.

[17] S. Gustavsson, J. Bylander, F. Yan, W. D. Oliver, F. Yoshihara, and Y. Nakamura, Noise correlations in a flux qubit with tunable tunnel coupling, Phys. Rev. B **84**, 014525 (2011).

[18] F. Yoshihara, Y. Nakamura, and J. S. Tsai, Correlated flux noise and decoherence in two inductively coupled flux qubits, Phys. Rev. B **81**, 132502 (2010).